

PAPER • OPEN ACCESS

Deconfinement of runaway electrons by local vertical magnetic field perturbation

To cite this article: Someswar Dutta *et al* 2024 *Nucl. Fusion* **64** 096027

View the [article online](#) for updates and enhancements.

You may also like

- [Deconfinement transitions in a generalised XY model](#)

Pablo Serna, J T Chalker and Paul Fendley

- [SPINDOWN OF ISOLATED NEUTRON STARS: GRAVITATIONAL WAVES OR MAGNETIC BRAKING?](#)

Jan E. Staff, Prashanth Jaikumar, Vincent Chan et al.

- [Phases of gauge theories](#)

Michael C Ogilvie

Deconfinement of runaway electrons by local vertical magnetic field perturbation

Someswar Dutta^{1,*} , Deepti Sharma¹, R.L. Tanna^{1,3} , J. Ghosh^{1,2} and D. Raju^{1,2}

¹ Institute for Plasma Research, Bhat, Gandhinagar 382428, India

² Homi Bhabha National Institute (HBNI), Anushaktinagar, Mumbai 400094, India

³ Institute of Science, Nirma University, Ahmedabad 382481, Gujarat, India

E-mail: sdutta@ipr.res.in

Received 30 January 2024, revised 27 May 2024

Accepted for publication 20 June 2024

Published 2 August 2024



Abstract

Runaway electron (RE) deconfinement and subsequent suppression is of prime importance for successful long-term operation of any tokamak. In this work, to deconfine and mitigate REs, the efficacy of local vertical field (LVF) perturbation has been explored numerically. LVF perturbation-assisted RE loss studies are carried out by simulating the drift orbits of the REs in magnetostatic perturbed fields and estimating the resulting orbit losses for different initial energies and magnitudes of LVF perturbation. To this end, the pre-existing PARTICLE code has been extended to the relativistic full-orbit-following code PARTICLE-3D (P3D) integrated with the magnetic field calculation code EFFI and plasma equilibrium field calculation code IPREQ to include the required fields for studying particle dynamics in general; this is then used to numerically model LVF perturbation-assisted RE deconfinement experiments conducted in the ADITYA tokamak. Simulation results show a significant ($\sim 90\%$) deconfinement of REs with the application of LVF perturbation of a suitable amplitude ($\sim 0.1\%$ of the total magnetic field) in a preferred direction. The existence of a threshold magnitude of the applied field is also established, which is observed to be dependent on the energy of the REs. The simulation results reproduce all the experimental observations and reveal other interesting features of RE mitigation using LVF perturbation. The temporal map of orbiting time of REs shows that REs originating from the inboard side edge region ($\psi_N > 0.5$) of the plasma are relatively more prone to be lost with the application of suitable LVF perturbation than those originating from the plasma core. Interestingly, the simulation results demonstrate the existence of strong correlation between the safety factor (q) profile in the plasma edge region ($\psi_N > 0.7$) and the level of RE deconfinement using LVF perturbation.

Keywords: runaway electrons, RE deconfinement, LVF perturbation, PARTICLE-3D

(Some figures may appear in colour only in the online journal)

* Author to whom any correspondence should be addressed.



Original content from this work may be used under the terms of the [Creative Commons Attribution 4.0 licence](#). Any further distribution of this work must maintain attribution to the author(s) and the title of the work, journal citation and DOI.

1. Introduction

Runaway electrons (REs) [1–6] are high-energy electrons that are generated in a tokamak under various scenarios such as initial plasma breakdown and the start-up phase [7], disruptions, high-energy neutral beam injection and high-power radio frequency heating. They can have a significant impact on plasma operation, making the study of RE dynamics an important area of research in the field of fusion energy. REs in a tokamak are of great concern irrespective of the size of the machine. It is well known that such REs, particularly in larger tokamaks where they carry a significant energy amounting to several MeV [1–7], can severely damage the first wall and in-vessel components of the tokamak and can interfere with complex plasma phenomena such as plasma equilibrium, magnetohydrodynamic (MHD) instabilities and plasma disruption [1–3]. Therefore, mitigation and control of such REs are of great concern for reactors such as ITER [1, 2] and DEMO. Similarly, for reliable operation of smaller tokamaks such REs should be suppressed or extracted without affecting the plasma operation. There are several techniques that can be used to mitigate [1] the effects of REs in tokamaks, such as massive gas injection (MGI), shattered pellet injection (SPI) and gas puffing in several tokamaks including DIII-D, TEXTOR, JET [8], ASDEX Upgrade, Tore Supra [9], supersonic molecular beam injection in ADITYA [10], impurity injection [11], active magnetic field control with resonant magnetic perturbation field (RMP) [12–25] and with local vertical field (LVF) perturbation [26–28]. Of all the RE mitigation methods, active magnetic field control [12–28] has been demonstrated to be an effective technique for reducing the generation of REs during various phases of plasma operation in several tokamaks. For example, RMP-assisted RE mitigation experiments have been demonstrated in JT-60 in which REs were suppressed with high perturbation fields; in TEXTOR RMP [13–15, 18] is used to increase runaway losses and suppress runaway avalanches; and in Tore Supra application of an ergodic divertor resulted in increased RE losses [17]. Recently, both experimental and numerical modelling studies on RMP-assisted RE mitigation in pre-disruption and post-disruption phases of plasma discharges in ASDEX Upgrade [19, 20], COMPASS [21, 22], DIII-D [22, 23] and SPARC [23] demonstrated different proportions of RE mitigation. However, predictive modelling studies for ITER [19] and SPARC [23] and experimental observations from JET [24] suggest that RMPs may not be effective in mitigating REs in larger tokamaks. Again, REs are successfully deconfined using LVF perturbation in VERSATOR-I [26] and in ADITYA [27, 28]. In all three phases of plasma operation, i.e. start-up, flat-top and ramp down phases of ADITYA plasma experiments, different levels (up to 90%) of RE deconfinement were achieved instantly with the application of LVF perturbation and the plasma performance was enhanced, as discussed in [27]. As plasma degradation is not of concern in the disruption phase, LVF perturbation-assisted RE mitigation may also be employed with a larger amplitude and pulse duration. Therefore, among the RE mitigation techniques, MGI and SPI are effective in disruption phases and have adverse effects on the plasma during

start-up or flat-top phases, while RMPs are somewhat effective in flat-top, pre-disruption and post-disruption phases in some tokamaks, but not so effective in larger tokamaks. On the other hand, although LVF perturbation-assisted RE mitigation has only been experimentally demonstrated in smaller tokamaks [26–28] the technique has the potential to be used in combination with other mitigation techniques to enhance RE losses before they achieve higher energies in larger tokamaks including ITER and DEMO. The cause of the differing success in suppressing and deconfining REs among devices remains unclear and more research is required in this field. Theoretical work has shown that strong radial diffusion of REs can prevent avalanches and estimated the necessary magnetic perturbation level to be $\delta B/B = 10^{-3}$ for typical tokamak parameters [29]. However, the radial diffusion coefficient is uncertain and depends on several factors. The simplest understanding is that electrons follow stochastic magnetic field lines and diffuse radially using the Rechester–Rosenbluth diffusion coefficient [30]. Recently, using the same underlying physics, the transport mechanism of REs in ADITYA [31] has been explained to some degree. This involved an upper limit; actual runaway confinement is usually better due to the finite Larmor radius and magnetic drift effects that reduce the diffusion coefficient and were not taken into consideration in [30] and [31] when explaining the complex transport mechanism of REs in a tokamak. A comprehensive understanding of the intricate impact of magnetic drifts on diffusion and transport of REs is achievable only through 3D numerical modelling of the electron drift orbits, as pointed out in [18, 25].

Although many simulation studies have been carried out to understand the RMP-assisted loss mechanism and deconfinement of REs in tokamaks as detailed above, similar in-depth simulation studies of LVF-assisted deconfinement of REs are not available except for a mention of preliminary modelling using field lines in [26]. As the drift orbit topology is significantly different from the intricate stochastic field line behaviour inside a tokamak, it is necessary and important to model LVF-assisted deconfinement numerically using drift orbit topology analysis. Therefore, to serve this purpose a code needs to be developed.

To date several numerical codes have been developed for studying the complex RE dynamics in a tokamak [18–23, 25, 32–44]. These can be roughly classified based on the numerical methods adopted, the number of degrees of freedom chosen, the type of radiation and collisional losses incorporated and the inclusion of self-consistent coupling between the electric and magnetic fields of the plasma. Particle-based methods track RE trajectories and incorporate collisional transport using Monte Carlo techniques, while continuum methods solve partial differential equations (Fokker–Planck equation) for RE distribution functions. The number of degrees of freedom incorporated in RE dynamics studies can vary based on physical considerations and computational limitations. The simplest models track only parallel and perpendicular momentum, while more advanced models incorporate radial and spatial degrees of freedom to model the Lorentz force, and the number of degrees of freedom incorporated is considered to be the most important physical and

computational element in numerical studies of RE dynamics. A detailed discussion on the different approaches to numerical modelling of RE dynamics is given in [45]. Although the self-consistent electric and magnetic fields may have a significant role to play in RE dynamics, as pointed out in [19–23, 25], it is beyond the scope of the present work to incorporate such a physical description in our simulation studies. In previous studies it was found that the effect of radiation losses on RE dynamics is only significant for REs with very high energies above 50 MeV [18, 25, 45], and the RE energy considered here for RE deconfinement studies in ADITYA would be a maximum of ~ 5 MeV [27, 28, 31]; therefore the radiation loss effect on the RE dynamics would be insignificant and hence is not incorporated in the present computations. Also, the RE dynamics is practically collisionless as the time scale of observation for the present case study is $t \sim 10^{-7}$ – 10^{-4} s, which is much smaller than the relativistic electron collision time scale of 10^{-2} s [45]. It is also found that the RE losses are mainly dominated by the drift orbit losses and collisional loss is not very significant [18, 25]; therefore collisional effects are not included in the simulation results presented here.

In the present work, a particle-based approach [42–45] is used to model the exact relativistic Lorentz force in six-dimensional (6D) phase space due to its numerical implementation and parallelization advantages to study the drift orbit losses of the REs. To avoid potential limitations of reduced degree of freedom descriptions in accommodating the vast difference between the spatio-temporal scales of the gyro-period $t \sim 10^{-11}$ s and the observational time scales $t \sim 10^{-7}$ – 10^{-4} s, a relativistic full orbit following code PARTICLE-3D (P3D), based on the pre-existing non-relativistic code PARTICLE [46], has been developed to study the space-dependent 3D magnetic effects on RE dynamics. P3D is capable of taking plasma equilibrium fields as input through g-files, and can thus take equilibrium fields from any equilibrium code that generates the output file in the standard g-file format. Here IPREQ [47, 48] code-generated equilibrium fields for ADITYA are included to study the RE dynamics. Other than the plasma equilibrium fields, the P3D code is integrated with the EFFI code [49] to incorporate accurate 3D fields from various actual 3D coils with a finite cross section. EFFI-generated fields from toroidal field (TF) coils, poloidal field (PF) coils, ohmic transformer coil sets and perturbation field coils may be used as per the simulation set-up requirements. Apart from that, prescribed electric and magnetic fields from other sources can also be incorporated in the simulations as required. P3D has several stopping criteria to stop the 3D tracking of the charged particle based on the prescribed time, toroidal transit, poloidal transit and loss to the wall, which can be used in combination as per the simulation set-up requirements. Finally using the P3D code, an attempt has been made to numerically model RE deconfinement experiments using the LVF coil in ADITYA with a focus on understanding the RE dynamics under the influence of LVF perturbation and its dependence on the perturbation direction and amplitude and energy of the REs by analyzing the drift orbit topology using tools such as the Poincaré section plot, loss fraction study and temporal maps of time of flight.

The present article is organized as follows: section 2 describes the experimental set-up and observation of the experiments conducted. Section 3 explains the numerical modelling techniques for the relativistic charged particle dynamics adopted in P3D along with the theoretical benchmarking. The effects of LVF perturbation on RE dynamics are numerically modelled and analyzed in section 4. In section 5, RE deconfinement experiments conducted in ADITYA are modelled and the subsequent simulation results are discussed. Finally, a summary and conclusions are presented in section 6.

2. Experimental set-up and observation in ADITYA

RE trajectories in a tokamak are greatly affected by the magnetic field topology they experience inside the tokamak. The field topology is formed by a combination of several external coil-generated fields at the beginning and is later dominated by the equilibrium field generated by the plasma current during the plasma discharge phase. The resultant magnetic field topology, which influences the RE trajectories, is formed by the combination of these two magnetic field configurations including the external LVF perturbation.

2.1. Description of the ADITYA coil systems

ADITYA [27, 28] is a mid-sized air-cored tokamak having major radius $R_0 = 0.75$ m and minor radius, $a = 0.25$ m with circular limiter configuration. The ADITYA coil system consists of an Ohmic coil system, PF coils, vertical field coils and TF coils. For typical plasma discharges in ADITYA, a toroidal magnetic field of 0.75–1.5 T at the major radius $R_0 = 0.75$ m is used. To extract the REs, the LVF coils comprise a pair of up-down symmetric coils placed at radial distance R_{LVF} at the top and bottom in between TF coil I-beams 1 and 2 of ADITYA [27, 28]. A schematic of the Helmholtz-like configuration of the LVF coil system is shown in figure 1 and the detailed configuration of the LVF coils along with the other coils is discussed in [28]. The LVF coil parameters of ADITYA are summarized in table 1.

2.2. Experimental set-up and experimental observations

As detailed in [27], RE deconfinement experiments were carried out with typical hydrogen plasma discharges in ADITYA, having plasma parameters such as plasma current ~ 70 – 90 kA, toroidal magnetic field $B_\phi \sim 0.75$ – 0.85 T, edge safety factor $q_a \sim 2.5$ – 6 , discharge duration ~ 80 – 100 ms, average central electron density $n_e \sim 1$ – 2×10^{19} m $^{-3}$ and central electron temperature $T_e \sim 300$ – 450 eV. LVF coils are installed with the configuration shown in figure 1 at one toroidal location. LVF coils are connected in series to produce LVF perturbation in the opposite direction to the actual equilibrium field. A NaI scintillation detector is placed in front of the limiter to monitor the hard x-ray (HXR) emissions from the experiments. RE deconfinement experiments were carried out in the initial phase, current ramp-up phase and termination phase. In the experiments, 5–20 ms short pulse LVF perturbations were

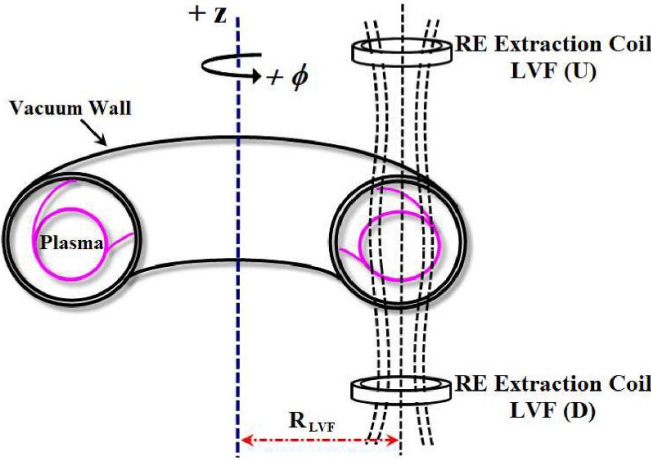


Figure 1. Schematic of the Helmholtz-like local vertical field (LVF) coil configuration used for magnetic extraction of REs in ADITYA [27]. Reproduced from [27]. © 2015 IAEA, Vienna. All rights reserved.

Table 1. LVF coil parameters, radius (R), vertical distance (Z), radial width (dR) and vertical width (dZ) of ADITYA [27, 28].

Coil type	R (m)	Z (m)	dR (m)	dZ (m)	No. of turns	Current (kA)
LVF(U)	0.2335	0.8000	0.0430	0.0850	± 50	4.3
LVF(D)	0.2335	-0.8000	0.0430	0.0850	± 50	4.3

applied with varying magnitude from 150 to 260 G for RE deconfinement purposes.

A significant reduction (about five times) in HXR emissions was observed in the initial phase of discharges in which the LVF perturbation was applied (shot #24976, 5–10 ms) compared with the case when LVF was not applied (shot #24969), as shown in figure 2. Similarly, for other plasma shots different degrees of RE deconfinement characterized by a reduction in the HXR signal were observed, with the application of LVF perturbation as detailed in [27]. Therefore, with the application of a LVF perturbation significant reduction of HXR emission over time is observed, which means that the REs are extracted from the plasma before gaining higher energies without affecting the thermal component of the plasma in typical ADITYA discharges. Without the LVF, HXR emission continues for longer during the breakdown and current ramp-up phases. However, HXR emission ceases once the LVF is applied. This extraction mechanism of REs is explained in [27] on the basis of radial diffusion governed by the applied LVF perturbation.

A list of ADITYA plasma discharge shot numbers is given in table 2 in which different levels of RE deconfinement are observed.

To model these experiments, and to carry out the required simulation studies, the IPREQ-generated plasma equilibrium magnetic flux configurations along with the up and down LVF coil-generated (coils placed at R_{LVF} and the $\phi = 0$ plane) perturbation fields calculated by the EFIGI code need to be incorporated into the simulation code described later. IPREQ-generated plasma equilibria and the field line traced safety

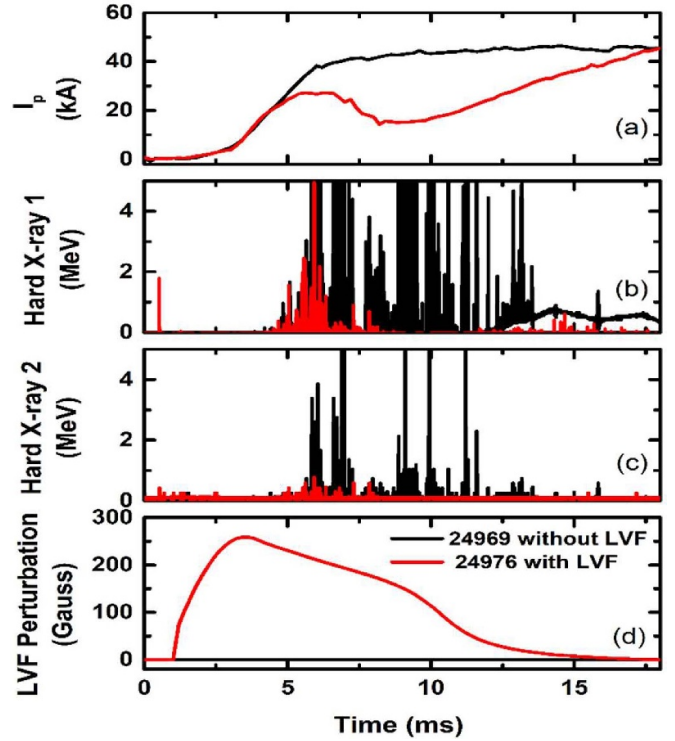


Figure 2. ADITYA plasma discharge comparison with LVF (shot #24976 red) and without LVF (shot #24969 black), showing temporal evolution of (a) plasma current, (b) hard x-ray signal from the 3-inch detector, (c) hard x-ray signal from the 1.5 -inch detector and (d) LVF perturbations for magnetic extraction of REs in the initial phase [27]. Reproduced from [27]. © 2015 IAEA, Vienna. All rights reserved.

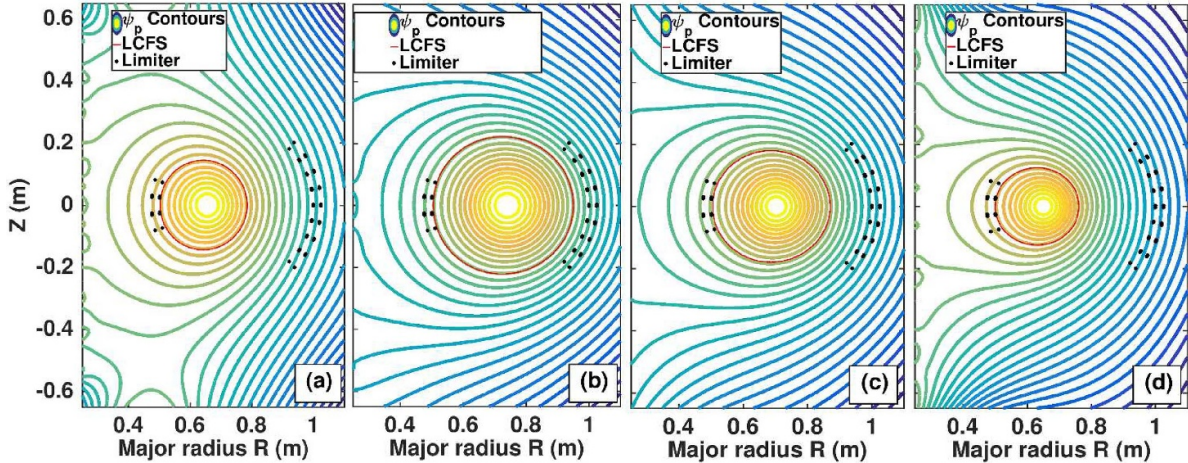
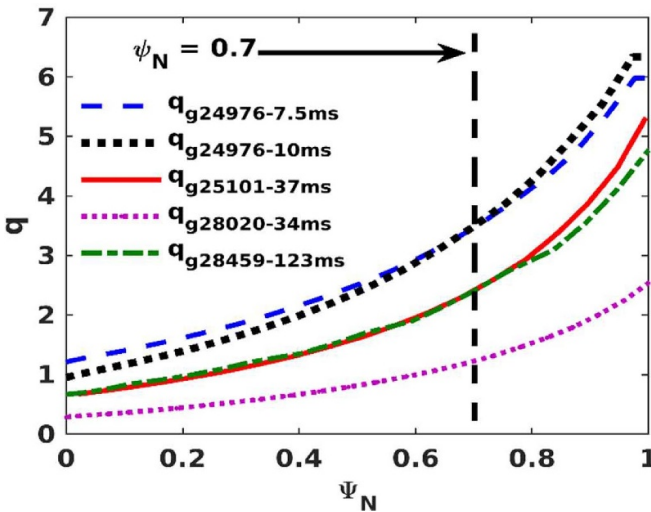
factor (q) profile for the ADITYA plasma discharges are shown in figures 3 and 4, respectively. The edge safety factor q of these equilibria is in the range of 2.5–6. To start with, discharge #25101 is analyzed in detail to understand the effect of LVF perturbation on the RE dynamics. Finally, loss fraction studies for all other plasma equilibria are considered in later sections. The simulation studies presented here assume that a sufficient number of REs are present in the plasma prior to the application of LVF perturbation and their subsequent mitigation upon application of the LVF pulse. Note that generation of REs through any mechanism during the LVF pulse is not considered in the simulation.

3. Relativistic model equations and numerical methods

REs can have energies of several MeV, and therefore such electrons are subjected to the relativistic Lorentz force along with the relevant radiation losses as described in detail in [45]. For typical ADITYA plasma discharge parameters, $R_0 = 0.75$ m, $a = 0.25$ m, $B_0 = 0.85$ T, $q_a \sim 3$ along with the electronic mass m_e , charge e and velocity of light c , the maximum attainable energy [50] of REs during the start-up phase, corresponding to $I_p \sim 30$ kA, and flat-top phase, corresponding to $I_p \sim 90$ kA, can be estimated by $E_{\text{Max}}^{\text{rf}} \approx (56R_0I_p \text{ (MA)})/a \times$

Table 2. Experimental setup for RE extraction experiments in ADITYA [27].

Item	Shot 24976, 7.5 ms start-up	Shot 25101, 37 ms flat-top	Shot 28020, 34 ms flat-top	Shot 28459, 123 ms ramp-down
Direction and amplitude of B_T at $R_0 = 75$ cm	$+ \phi$ $B_T = 0.8$ T	$+ \phi$ $B_T = 0.8$ T	$+ \phi$ $B_T = 0.85$ T	$+ \phi$ $B_T = 0.85$ T
Direction and amplitude of plasma current I_p	$- \phi$ $I_p \sim 22.08$ kA	$- \phi$ $I_p \sim 70.20$ kA	$- \phi$ $I_p \sim 91.20$ kA	$- \phi$ $I_p \sim 26.20$ kA
Direction of vertical field B_v	$+Z$	$+Z$	$+Z$	$+Z$
Direction of LVF used	$-Z$	$-Z$	$-Z$	$-Z$
Direction of RE velocity	$+ \phi$	$+ \phi$	$+ \phi$	$+ \phi$

**Figure 3.** Equilibrium poloidal flux contours for four different ADITYA tokamak plasma shots: (a) 24976 at 7.5 ms during start-up, (b) 25101 at 37 ms during flat-top, (c) 28020 at 34 ms during flat-top and (d) 28459 at 123 ms during the ramp-down phase.**Figure 4.** Variation of safety factor q of four different plasma shots with normalized poloidal flux.

$m_e c^2 \sim 2.6\text{--}7.7$ MeV, while the maximum attainable energy of REs during disruptions [18, 25] can be estimated by $E_{\text{Max}}^d \approx (eca^2 B_0 / q_a R_0 e) \times 10^{-6} \sim 7.1$ MeV. As mentioned in the previous section, in the cases analyzed here the maximum energy of the REs would be ~ 5 MeV, therefore the radiation loss mechanism does not make a significant contribution to the RE

dynamics and the relativistic Lorentz force component would suffice to study the drift orbits of REs in the present case studies. The relativistic Lorentz force can be written as

$$\frac{dx}{dt} = v \quad (1)$$

$$\frac{dp}{dt} = -e [E(x) + v \times B(x)] \quad (2)$$

where x is the position and v the velocity of an electron with charge e and mass m_e and $p = \gamma m_e v$ is the relativistic momentum with Lorentz factor $\gamma = (1 - v^2/c^2)^{-1/2}$. E and B are the relevant electric and magnetic fields for studying a particular physical phenomenon. In the present case studies no electric field is considered and the particle dynamics studied here have a magnetic field configuration that is magnetostatic in nature, as discussed earlier in the introduction. In P3D simulations, a magnetic field corresponding to plasma equilibrium is used from the IPREQ-generated equilibrium for plasma shot #25101 and the LVF perturbation fields are included via EFFI-calculated fields with the LVF coil specifications given in table 1.

The P3D code is written in cylindrical geometry (R, ϕ, Z) to easily capture the symmetry of the tokamak, and equations (1) and (2) are solved in cylindrical geometry (R, ϕ, Z) using an advanced leap-frog scheme, the Vay integrator [45, 51]. In cylindrical geometry, for a pure magnetic field the relativistic energy $E = \gamma m_e c^2$ and the canonical conjugate momentum

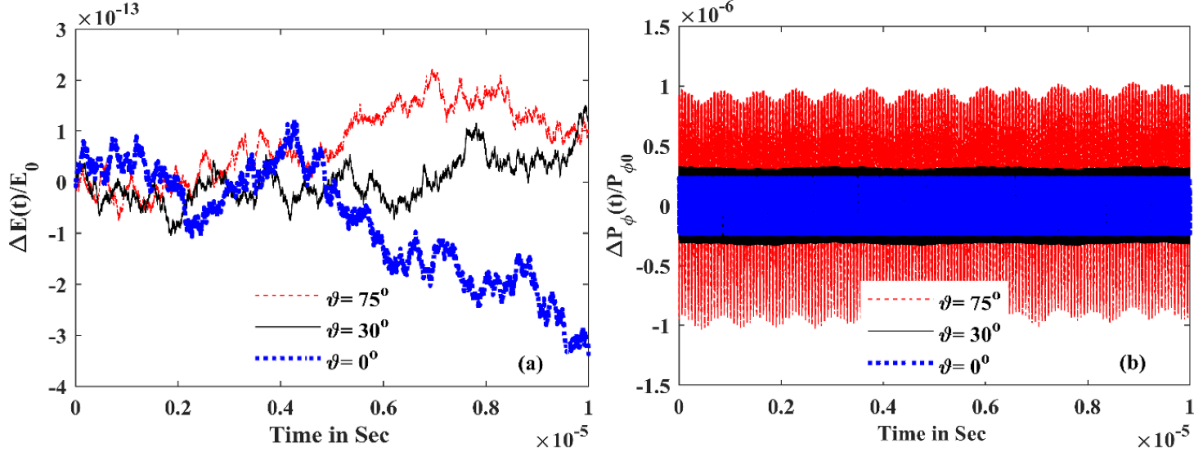


Figure 5. Time evolution of (a) relativistic energy fluctuation and (b) conjugate momentum fluctuation for 3 MeV REs tracked by the PARTICLE-3D code for 10 μ s with three different pitch angles.

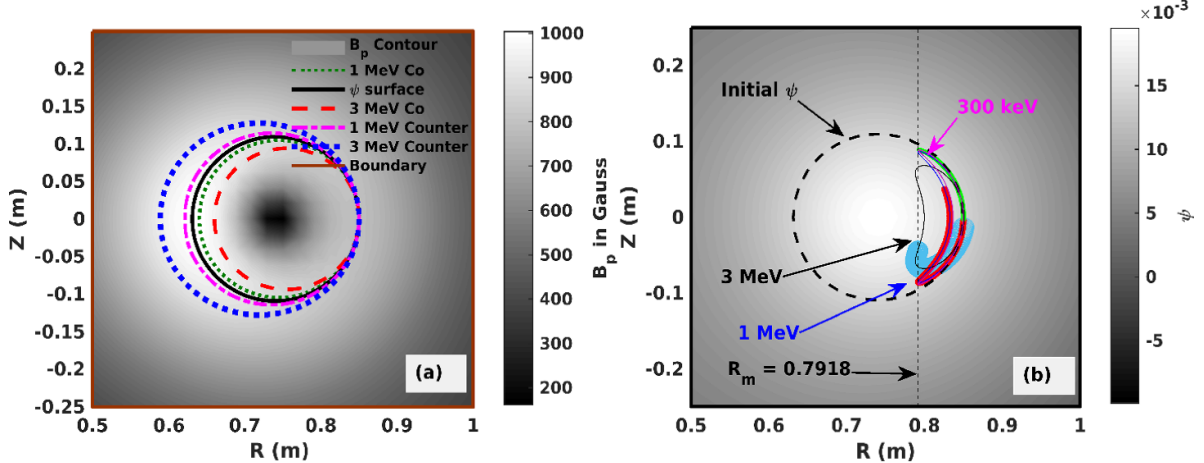


Figure 6. (a) 2D drift orbits of 1 and 3 MeV REs for both co- and counter-passing configurations along with the equilibrium flux surface traced by the field line (black line), on the background of an equilibrium poloidal field. (b) Banana orbits of 300 keV and 1 and 3 MeV co-passing REs with the background of an equilibrium poloidal flux. The mirror point R_m for banana orbits is derived from the P3D simulation with a high degree of accuracy.

$p_\phi = \gamma m_e R v_\phi - q\psi$, where q is the charge and ψ is the magnetic flux, of the charged particle would be conserved. In the simulations, full orbits of the REs are resolved with selection of the time interval $dt = T/100$, where $T = 2\pi/\omega$ with $\omega = eB_0/\gamma m_e$ is the relativistic gyrofrequency, which ensures higher accuracy of the code output. Furthermore, to study the trapped particle dynamics, the amplitude of the perpendicular velocity component v_\perp is incorporated through pitch angle $\vartheta = \sin^{-1}(v_\perp/v)$ in the code. Therefore, the fluctuations in relativistic energy E and canonical conjugate momentum p_ϕ are obtained for REs with different initial conditions in a pure magnetic field configuration of the plasma equilibrium field to check the stability of the code, as shown in figures 5(a) and (b).

It is evident from figures 5(a) and (b) that the time evolutions of energy fluctuation and canonical momentum fluctuation are extremely small, at 10⁻¹³ and 10⁻⁶, respectively, ensuring excellent energy and momentum conservation properties of the P3D code for both passing and

trapped (pitch angle $\vartheta = 75^\circ$) REs in the symmetrical plasma equilibrium field. Such conservation properties are in good agreement with the previously reported results [45].

To see the particle drift orbit topology and how that differs from the field line topology for the same equilibrium field, the co-passing and counter-passing orbit topologies of the REs are simulated using P3D, as shown in figure 6(a). It is clear that the black line, which is a field line traced on the plasma equilibrium surface, is exactly on that equilibrium surface whereas the RE orbits that start from the same location do not coincide with that or any other plasma surfaces. The co- and counter-passing RE orbits follow different paths for the same energy; the co-passing orbit shrinks the orbit volume on the inboard side while the counter-passing orbit does the opposite, i.e. it expands on the inboard side. Also, it is observable that with higher energy, their shrinkage or expansion is higher as per the velocity direction.

The best way to benchmark the particle drift in the geometry of a tokamak under the influence of an equilibrium field is to simulate the banana orbit and match the mirror point with the theoretically obtained value. Therefore, REs with three different energies (300 keV, 1 MeV and 3 MeV) were launched from an outboard side location $R = 0.85$ m, with the same pitch angle $\vartheta = 75^\circ$, and followed for one poloidal transit to record the mirror points. The banana orbits for three different energies are shown in figure 6(b). The mirror point obtained from the simulation (~ 0.7918 m) is in good agreement with the theoretical mirror point estimation given by $R_m = R_i \sin^2 \vartheta \sim 0.7930$ m, where $R_i = 0.85$ m is the starting point of the RE in the low-field side. We can therefore conclude that P3D is capable of accurately capturing the complex combined particle drifts with high accuracy and thus can be entrusted to simulate the drift orbits of REs in different magnetic field configurations.

It is clear from this study that the drift orbit topology is entirely different from the field line topology, therefore the simulation study carried out in [26] to understand the phenomenon of RE deconfinement is incomplete. Hence, in the next section, simulation results for RE deconfinement studies are presented with drift orbit topology analysis and discussed.

4. Effect of LVF perturbation on RE dynamics

Experimental observations in ADITYA show that application of a suitable LVF perturbation resulted in significant suppression of REs for most of the plasma phases, as described in detail in section 2. Interestingly, it is observed that both the amplitude and direction of the applied LVF perturbations play a significant role in the suppression of REs. However, in some plasma shots RE suppression was not that significant even with higher LVF perturbations [27]. In order to understand these experimental observations, simulation studies were carried out to obtain the effect of particle energies, pitch angles and positions on the RE dynamics and the subsequent deconfinement and losses of the REs in the magnetostatic equilibrium configuration for different levels of LVF perturbation.

As detailed in section 2, the plasma equilibrium for plasma shot #25101 is chosen for modelling of the RE deconfinement experiment along with different LVF currents and directions. To understand the effect of LVF perturbation, a radial distance of the LVF coil $R_{\text{LVF}} = 75$ cm is considered for the simulation studies in this section. Later, $R_{\text{LVF}} = 87$ cm is also considered for the loss fraction studies corresponding to the experimental set-up in the plasma shots discussed in the subsequent section. Depending upon the need to see a particular phenomenon, the tracking time and poloidal or toroidal transit of the REs are specified and used in the P3D simulations.

4.1. LVF perturbation and energy of the REs

The best numerical diagnostic for understanding and observing the effect of perturbation field and the subsequent drift orbit topology is the Poincaré section plot of the REs. Therefore, to gain detailed information about the effect of

LVF perturbation on plasma equilibrium, 3 MeV REs were tracked for 60 poloidal transits to produce the Poincaré section plots for three different cases of LVF perturbation, as presented in figure 7.

It is clear from figure 7 that for both positive (figure 7(a)) and negative LVF (figure 7(c)) cases the perturbation field breaks the symmetry of the drift orbits obtained for the no LVF case (figure 7(b)). In the case of negative LVF (figure 7(c)) confinement zone shrinkage takes out the REs in the outer plasma region towards the edge of the plasma, while in the positive LVF case (figure 7(a)) the drift orbit topology is strikingly different from that of the negative LVF case. The expansion of the confinement zone for positive LVF, shrinking of the confinement zone for negative LVF and, for both cases, merging and bunching of the drift orbits for 3 MeV REs in the inboard side of the plasma region are clearly observable from the poloidal view of the Poincaré section plots in figure 8. The phenomenon of expansion and shrinkage of the confinement zone in positive and negative LVF perturbation cases, respectively, is due to the alteration of particle drifts caused by the application of the LVF perturbations. For positive LVF perturbations, the particle drift towards the inner equilibrium surfaces gets reduced and the REs suffer larger poloidal orbit excursions and cover a larger area, thereby causing expansion of the confinement zone. For the negative LVF case, however, the REs experience more inward drifts due to the resultant total magnetic field, which reduces the poloidal orbit excursions thereby causing shrinking of the confinement zone. It is quite clear from this study that the direction of the LVF perturbation plays a significant role in the RE dynamics and the drift orbit rearrangements are strikingly different for positive and negative LVF perturbations.

As in the case of 3 MeV REs, expansion and shrinkage of the confinement zone and bunching of the drift orbits are also observed for the lower-energy 1 MeV REs (see figure 9). Shrinkage of the confinement zone of drift orbits for 1 MeV REs with negative LVF in figure 9(c) is smaller than for the 3 MeV REs in figure 7(c). The degree of breakage and merging of the drift surfaces is different for 1 MeV REs than for 3 MeV REs. Also, the expansion of the confinement zone on the inboard side of the plasma is clearly visible in figure 9(a) for positive LVF case. Therefore, it is evident that the energy of the REs plays a significant role in the drift orbit topology and subsequent extraction of such REs.

To understand the effect of the LVF perturbation amplitude on the RE dynamics in plasma, three different levels of negative LVF perturbations generated with three different LVF coil input currents (1.36 kA, 2.3 kA and 4.3 kA) are used to obtain Poincaré section plots for 1 MeV REs. The simulation results in figure 10 show that, with increasing perturbation, shrinkage of the confinement zone increases, but the bunching and rearrangements of the drift orbit topology for the three different cases are different and complex. With higher-amplitude LVF perturbation breaking of the inner drift surfaces is observable from figure 10(c). It is also observable from figures 10(b) and (c) that the REs from the inner region of the plasma escape their orbit and migrate to the outer region of the plasma and then some of the REs from the outer region are lost

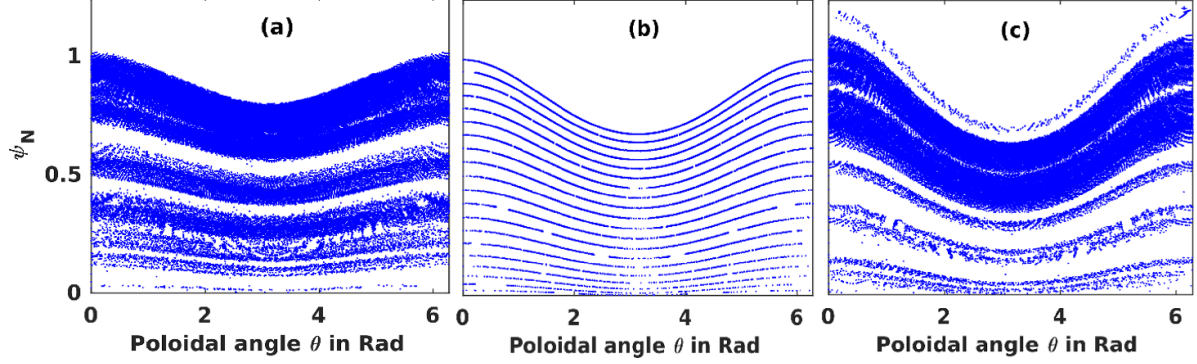


Figure 7. Poincaré section plot of drift orbits of 3 MeV co-passing REs with (a) positive LVF, (b) no LVF and (c) negative LVF perturbation of ~ 256 G at the major radius R_0 , generated by 4.3 kA of current in the LVF coils (50 turns).

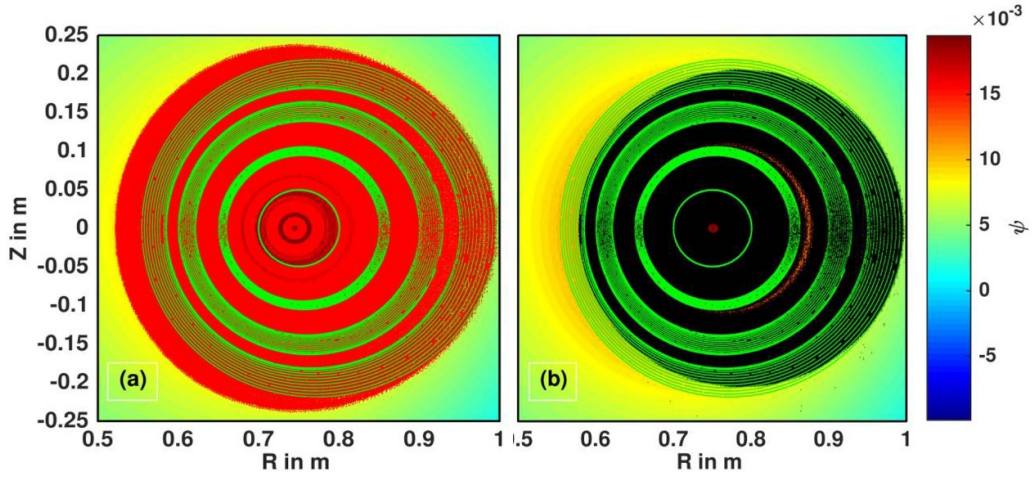


Figure 8. Poloidal view of Poincaré section plot of drift orbits for 3 MeV co-passing REs with (a) positive LVF (red) and no LVF (green) and (b) negative LVF (black) and no LVF (green). The LVF perturbation generated by 4.3 kA of current in the LVF coils (50 turns) is shown for both positive and negative configurations.

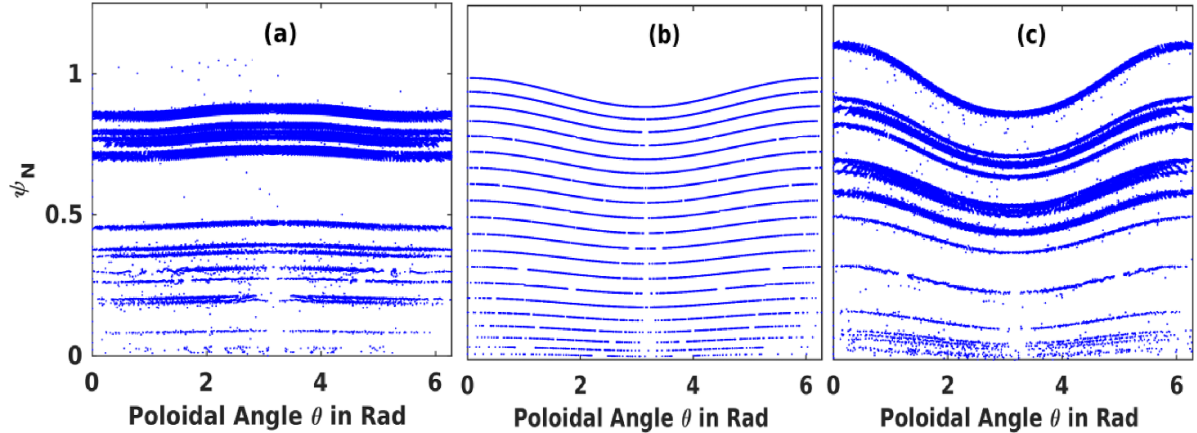


Figure 9. Poincaré section plot of drift orbits of 1 MeV co-passing REs with (a) positive LVF, (b) no LVF and (c) negative LVF perturbation generated by 4.3 kA of current in the LVF coils.

to the boundary as well. These simulation results illustrate that LVF perturbation amplitude and direction along with particle energy play important roles in the resultant RE dynamics and are crucial in explaining the experimental observation of RE deconfinement with the application of LVF perturbation.

4.2. Pitch angle of the REs

Another aspect of the study of RE dynamics is the role of pitch angle in the resultant drift orbit topology in combination with the RE energy and LVF perturbation. Although the

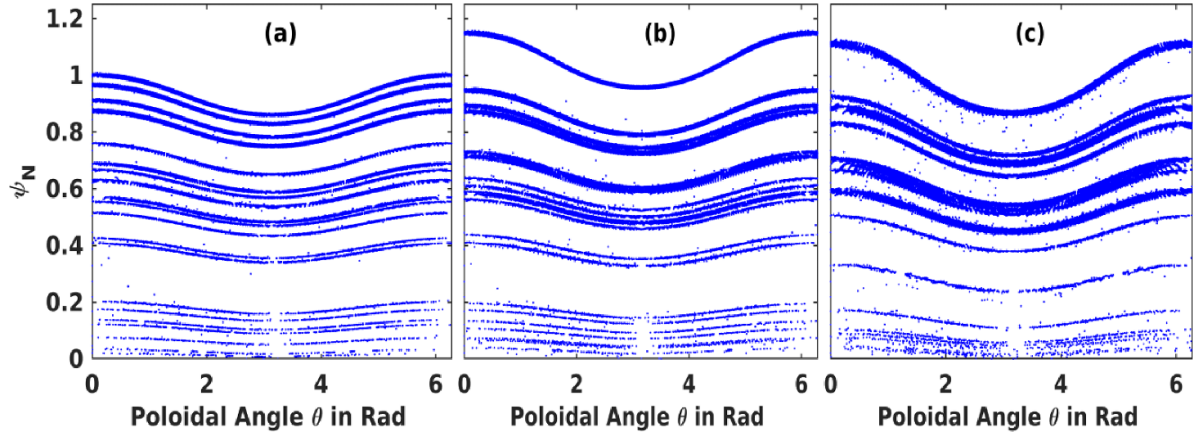


Figure 10. Poincaré section plot of drift orbits of 1 MeV co-passing REs with three different negative LVF perturbations generated by three different currents (a) 1.36 kA, (b) 2.3 kA and (c) 4.3 kA.

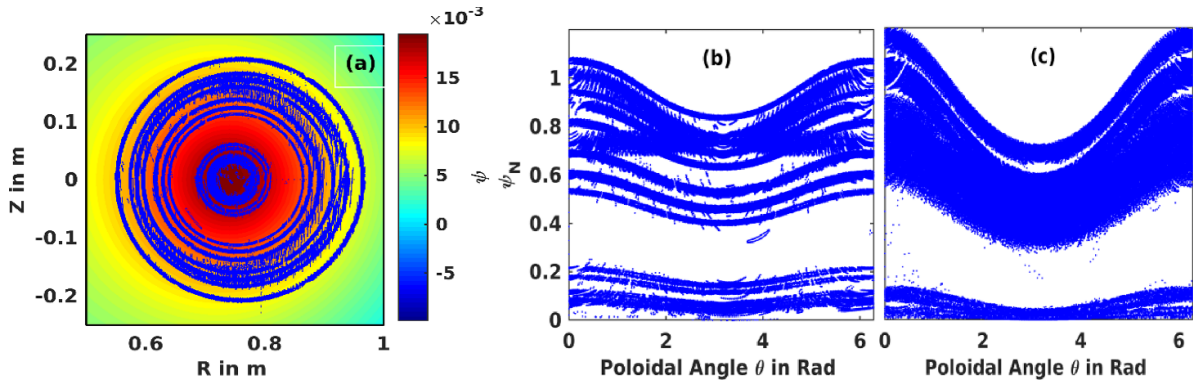


Figure 11. Poincaré section plot of drift orbits of REs with 30° pitch angles from (a) poloidal view for 1 MeV and standard view for (b) 1 MeV and (c) 3 MeV energies. Negative LVF perturbation generated by 4.3 kA of current is used for these case studies.

significance of the pitch angle is mostly associated with the synchrotron radiation loss and damping of high-energy REs (>50 MeV) with higher pitch angle ($>40^\circ$) [18, 25, 45], in the present case studies of relatively low-energy REs (<6 MeV) with lower pitch angles ($<30^\circ$) in the collisionless regime ($t \sim 10^{-3}$ ms) it is important to understand the influence of pitch angle on the drift orbit topology of such REs. Therefore, to understand the effect of pitch angle ϑ on the drift orbit topology, REs of energies 1 MeV and 3 MeV with $\vartheta = 30^\circ$ are tracked to obtain the Poincaré section plot in the presence of negative LVF perturbation.

The simulation results in figure 11 show increased bunching and overlapping of the drift orbits for both 1 and 3 MeV REs with the application of a negative LVF perturbation. From figure 11(a) it can be observed that REs migrate from one drift surface to another in the top and bottom regions of the plasma, and there are plasma regions where there are no drift orbits at all. The impact of such complex drift orbit formations on RE deconfinement can only be understood from loss fraction study of the REs with different initial conditions. Therefore in the next section the RE loss fraction studies are presented and discussed.

5. LVF-assisted loss fraction studies

5.1. Direction and amplitude of LVF, RE energy and pitch angles

It is clear from the simulation results presented in the above sections that with increasing RE energy the confinement volume shrinks, leading to the loss of some REs to the boundary, which is a well-understood phenomenon. The shrinkage of the confinement zone is further modified due to the drift orbit dynamics under the influence of the right kind of external magnetic field perturbation, such as the application of negative LVF perturbations in the present case studies. In the case studies of RE dynamics reported earlier, with the application of RMP fields through RMP coils or dynamic ergodic divertor coils, the drift orbit topology responds to the type of RMP field applied and the REs from the outer plasma region $\psi_N > 0.5$ are most affected and get lost due to the modified drifts in the resultant stochastic structure of the plasma edge magnetic field configuration. However, here in the case of LVF coil lead perturbation it is clearly observable from figures 7–11 that the LVF perturbation does penetrate the plasma all the way to its

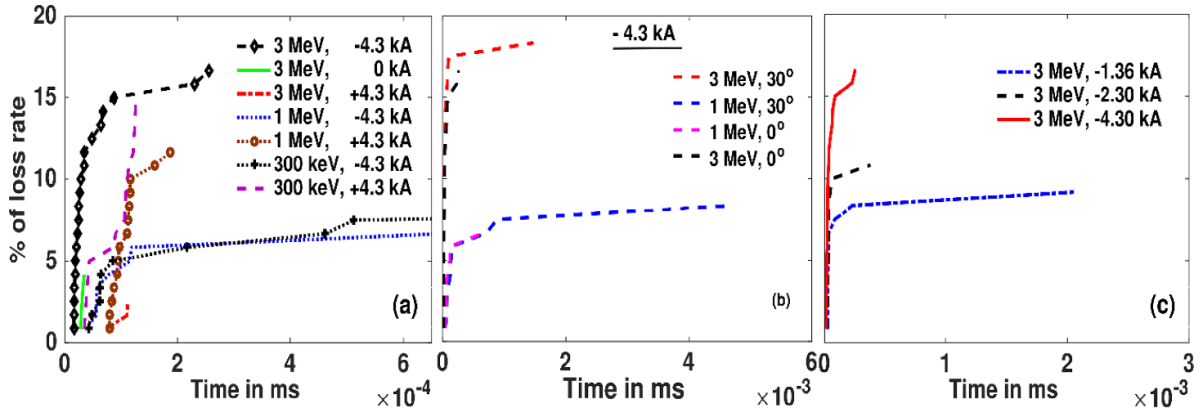


Figure 12. Loss fraction study for (a) 300 keV and 1 and 3 MeV REs with positive LVF, no LVF and negative LVF perturbation generated by a 4.3 kA current. (b) Different energies and pitch angles of REs with negative LVF perturbation by a 4.3 kA current. (c) 3 MeV REs for different negative LVF perturbations.

core region $\psi_N < 0.2$, and breaks the symmetry of the drift surfaces of the unperturbed case. Now, to understand the impact of this penetration of the LVF perturbations on the RE dynamics the subsequent loss studies are presented here.

To obtain the loss fraction of RE deconfinement, 120 REs [18] with 3 MeV energy are placed between the plasma core and the edge region in four different radial locations and followed for 60 poloidal transits in the absence and presence of a LVF perturbation field. Loss of a RE is recorded when a RE hits the boundary and the total orbiting time is recorded to generate a temporal map of REs on the poloidal plane.

Simulation results in figure 12(a) show that the direction of the LVF perturbation does play an important role in the RE deconfinement process, with the negative LVF perturbation-assisted loss fraction of 16.66% being more than four times higher than the no LVF case and more than six times higher than the positive LVF perturbation case, as shown in figure 12(a). The onset of loss of REs with the application of a negative LVF is in agreement with the experimental observation of RE deconfinement studies conducted in ADITYA as discussed in section 2.2.

To understand how the pitch angle affects the loss mechanism, 1 and 3 MeV REs with a pitch angle ϑ of 0° and 30° are tracked with the application of negative LVF perturbations. The simulation results show that in the presence of negative LVF perturbation for REs with a higher ϑ , the loss fraction slightly increases for all RE energies compared with REs with a pitch angle $\vartheta = 0^\circ$, as shown in figure 12(b). This phenomenon is likely to be attributable to two factors. Firstly, as the pitch angle increases, the Larmor radius of the REs also increases, leading to larger local excursions of the REs. Consequently, the REs become more susceptible to migration between different magnetic surfaces. Secondly, the resultant rearrangement of the complex particle drifts due to external perturbations allows them to migrate across the magnetic surfaces. As a result, there is a slightly higher loss of REs with higher pitch angles.

In figure 12(c), the simulation results of RE loss fraction studies are presented for 3 MeV REs under the influence of

three different LVF perturbation field amplitudes corresponding to LVF coil currents of 1.36 kA, 2.3 kA and 4.3 kA. It is evident from the results that an increase in the LVF perturbation current leads to an increase in the loss fraction of REs. Furthermore, the simulation reveals that REs with 1 MeV energy do not experience any loss at LVF perturbation currents below 4.30 kA. Similarly, REs with 300 keV energy exhibit very small loss within 60 poloidal transits, even at an LVF perturbation current of 4.30 kA. From these observations, it can be concluded that the lower cutoff for the amplitude of LVF perturbation current is strongly dependent on the RE energy. Therefore, higher LVF perturbation amplitudes are necessary to deconfine REs with lower energies. Consistent with these simulation findings, recent experiments conducted in ADITYA confirm the presence of a lower threshold of LVF perturbation current (> 1.7 kA) below which no deconfinement of REs is observed [28]. However, above this threshold, deconfinement of REs with energies ranging from 2 to 5 MeV are observed. Comprehensive loss fraction studies were conducted, considering various combinations of RE energy, pitch angle, LVF perturbation direction and amplitude, and the simulation results are summarized in figure 12.

5.2. Temporal map and the penetration depth of LVF perturbation

In connection with the presented loss studies, several intriguing questions arise regarding the specific region of the plasma from which REs are undergoing deconfinement, as well as the fate of REs originating from different regions within the plasma. In order to gain insights into these inquiries, the temporal distribution of the orbiting time of REs is examined for the simulation cases depicted in figure 12(a).

Figures 13(a)–(c) represent such temporal maps for the scenarios involving 3 MeV REs for a positive LVF perturbation with 4.3 kA, no LVF perturbation and a negative LVF perturbation with 4.3 kA, respectively. Additionally, figure 13(d) presents a temporal map for 300 keV REs with

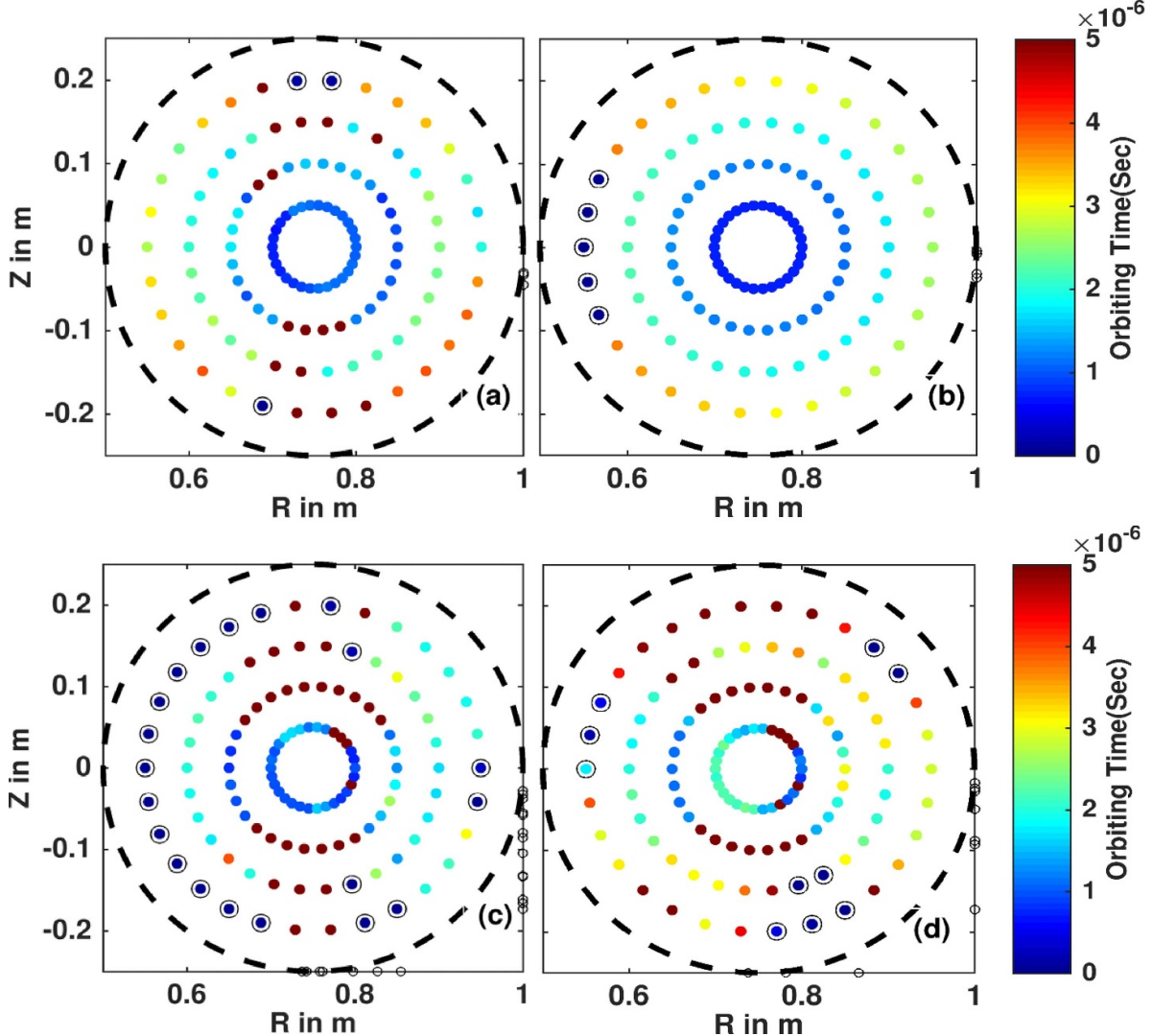


Figure 13. Temporal map of orbiting time in loss fraction studies with LVF perturbation of 4.3 kA for (a) 3 MeV REs with positive LVF, (b) 3 MeV REs with no LVF, (c) 3 MeV REs with negative LVF and (d) 300 keV REs with negative LVF. Positions encircled in black represent lost REs in all cases. Encircled points in the plasma region represent the deconfined REs and the empty circles on the rectangular boundary represent the footprints of such deconfined REs.

a similar simulation set-up to negative LVF perturbation with 4.3 kA. Analysis of figure 13 reveals that the deconfined REs (encircled) exhibit shorter orbiting times than other REs originating from the entire plasma region in their respective cases. Furthermore, a comparison of the orbiting times depicted in figures 13(a) and (c) with those in figure 13(b) shows that REs pulled towards the plasma edge demonstrate reduced orbiting times relative to their counterparts in the case of no LVF perturbation. Conversely, REs pushed towards the plasma core exhibit increased orbiting times compared with the corresponding REs in the absence of LVF perturbation. Figure 13(c) shows that the REs originating from the inboard side of the plasma region are most affected and exhibit deconfinement due to the negative LVF perturbation in contrast to the positive LVF case, where the REs located in the top and bottom of the plasma region are affected. Moreover, it is evident that the effective penetration depth of the negative LVF perturbation is greater than in the positive LVF case, as some REs from the

inner region of the plasma undergo deconfinement as a result of the negative LVF perturbation.

In order to understand why negative LVF perturbation is more effective for REs with relatively higher energy (>1 MeV) while positive LVF perturbation is effective for lower energies it is necessary to analyse the spatial distribution of these perturbations in relation to the total magnetic field (B_t) and the poloidal magnetic field (B_p). Here the total magnetic field B_t , which is a combination of toroidal field B_T and the plasma equilibrium field, is used to assess the relative strength of the perturbation field. The variations in the total magnetic field $\delta B_t/B_t$ (δB_t being the difference in B_t when the LVF perturbation is considered) and in the poloidal magnetic field $\delta B_p/B_p$ on the $\phi = 0$ plane are obtained for a negative LVF perturbation and presented in figures 14(a) and 15(a). Similarly, the corresponding variations for a positive LVF perturbation are shown in figures 14(b) and 15(b). Comparing the configurations of the

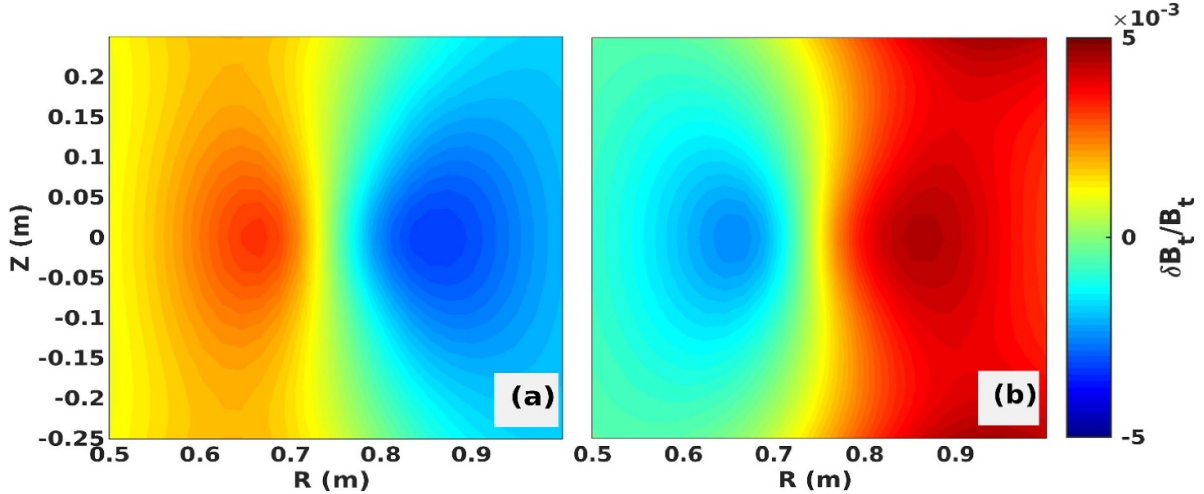


Figure 14. Contour plot of the change in total magnetic field $\delta B_t/B_t$ on the $\phi = 0$ plane for (a) a negative LVF perturbation of 4.3 kA and (b) a positive LVF perturbation of 4.3 kA.

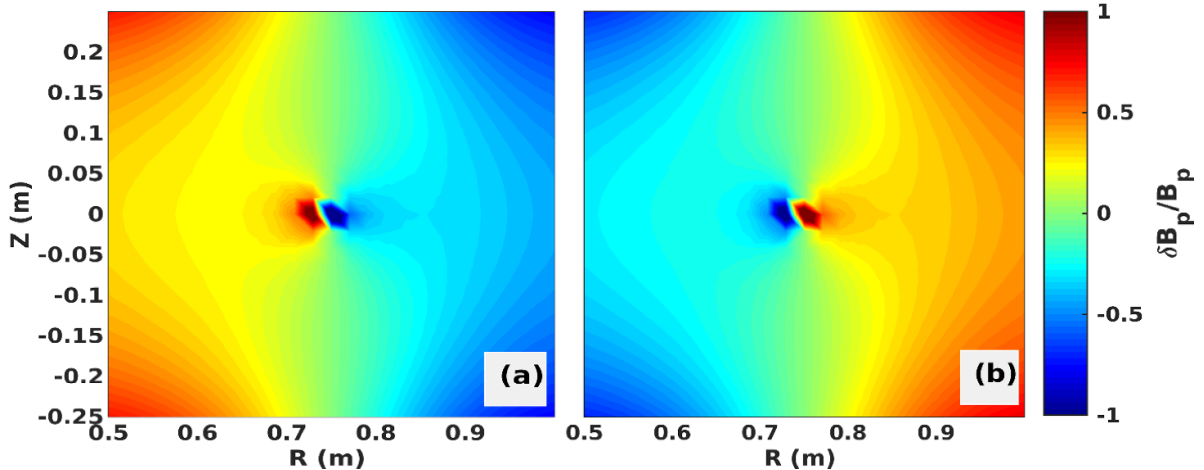


Figure 15. Contour plot of the change in poloidal magnetic field $\delta B_p/B_p$ on the $\phi = 0$ plane for (a) a negative LVF perturbation of 4.3 kA and (b) a positive LVF perturbation of 4.3 kA.

total and poloidal filed perturbations for the negative LVF case in figures 14(a) and 15(a) with their counterparts in figures 14(b) and 15(b) with positive LVF, it can be observed that the perturbation distributions in both total and poloidal fields are mirror opposites of each other. From figures 14(a) and 15(a) it is clear that there is a relatively stronger and positive $\delta B_t/B_t \sim 10^{-3}$ (equivalently $\delta B_z/B_T \sim 10^{-2}$) and $\delta B_p/B_p \sim 10^{-1}$ on the inboard (high- B_T) side of the plasma region for the negative LVF case compared with the outboard (low- B_T) region. This contributes to the higher effectiveness of negative LVF perturbation in deconfining the REs having relatively higher energies from the inboard region, as depicted in figure 13(c). The reason for this is that when high-energy REs travel from a region with a lower perturbation field to a region with a higher perturbation field they suffer relatively larger inward drifts and their orbits get compressed, but when they travel from a region with relatively higher perturbation field to one with a lower perturbation field their orbit expands and the REs hit the boundary and hence get deconfined (see figure 8(b)). In the case of a positive LVF, with the

relatively stronger and positive $\delta B_t/B_t$ and $\delta B_p/B_p$ on the outboard (low- B_T) plasma region, the low-energy REs (300 keV) starting from the outboard side exhibit deconfinement. The reason in this case is exactly opposite to that in the previous case; here the low-energy REs starting from the region with a relatively higher perturbed field (outboard side) would suffer outward drifts causing their orbits to expand (figure 8(a)), resulting in them hitting the boundary and hence becoming deconfined.

Therefore, the perturbation configuration in the negative LVF cases, in which the perturbation magnitude is high (low) on the inboard (outboard) side, results in a greater radial displacement of the high-energy REs, leading to their higher losses. In contrast, the perturbation configuration in the positive LVF cases, in which the perturbation magnitude is low (high) on the inboard (outboard) side, causes larger radial displacement of the low-energy REs, resulting in their higher losses. These findings highlight the significant role played by the LVF perturbation configuration in deconfining REs of varying energies from the tokamak plasma. These results will

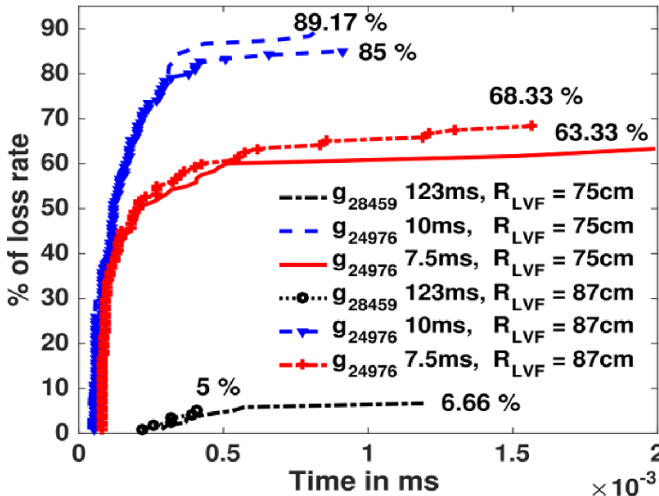


Figure 16. Loss fraction study of 3 MeV REs with negative LVF perturbation generated by 4.3 kA current with two different R_{LVF} positions and for three different plasma equilibria: shot 24976 at 7.5 ms, shot 24976 at 10 ms and shot 28459 at 123 ms.

also be useful in deciding the application of LVF polarity depending upon the energies of REs present in the discharge.

5.3. Influence of the safety factor (q) on RE losses

As previously discussed in section 2.2, RE deconfinement experiments (plasma shots #24976, #28020 and #28459) were conducted in ADITYA with negative LVF perturbations for different phases of the plasma shots, and different degrees of RE deconfinement were achieved in those experiments [27].

Although the LVF perturbations are created by the coils which are kept at a fixed location with respect to the major radius, the effect of such external perturbation would not be the same for different plasma equilibria for two reasons: firstly, because placement of the plasma equilibria inside the vessel differs for each case and secondly due to the unique plasma equilibrium feature, namely the safety factor q . The plasma equilibria considered here have different q profiles, as shown in figure 4 where it can be seen that the edge safety factors vary significantly between $q = 2.5$ and $q = 6$. Therefore, simulation studies are required to investigate the role played by the safety factor in such RE deconfinement experiments. Hence RE loss fraction studies are carried out taking into account the plasma equilibria of those experiments in the simulations. To model these RE deconfinement experiments, 120 REs of 3 MeV energy, originating from the plasma region $\psi_N \sim 0.7$, are tracked for 60 poloidal transits with a time limit of 2 μs under the influence of negative LVF perturbation with 4.3 kA for different plasma equilibria. Also, to explore the effect of LVF coil position on the RE loss fraction, $R_{LVF} = 75\text{cm}$ and $R_{LVF} = 87\text{cm}$ were considered for all the simulation studies presented in this section. Simulation results obtained for these loss fraction studies are presented in figure 16, where it can be seen that different levels of RE deconfinement resulted for different plasma equilibria in the corresponding plasma experiments.

The simulation results demonstrate a significant loss of ~90% of REs for the plasma equilibrium g-24976 at 10 ms, additionally, there are losses exceeding 60% at 7.5 ms, as depicted in figure 16. These findings align well with the corresponding experimental observations presented in figure 2, which depicts the absence of RE bursts for times between 7.5 ms and 10 ms. In contrast to that, for the plasma equilibrium g-28020 at 34 ms, the simulation shows no RE losses. However, the corresponding experiment indicates poor deconfinement of the REs, with the presence of several RE bursts, as shown in figure 5(h) in [27]. Similarly, for the plasma equilibrium g-28459 at 123 ms, the simulation results indicate a loss fraction of approximately 8% for 3 MeV REs. This finding correlates with the corresponding experiment, where the presence of low-energy (<3 MeV) RE bursts were observed and only high-energy REs were effectively suppressed at 123 ms, as illustrated in figure 6(a) of [27]. Furthermore, the RE loss rate is found to be sensitive to the radial location R_{LVF} of the LVF coils, as shown in figure 16. It is seen that case studies with $R_{LVF} = 87\text{cm}$ have a slightly lower loss rate compared with the $R_{LVF} = 75\text{cm}$ case. The perturbation magnitude and configuration are dependent on the radial position R_{LVF} of the LVF coils and the RE losses are dependent on the resultant perturbation magnitude and configuration in the plasma region, as discussed in the previous section. This explains why varying loss rates are obtained for different radial positions of the LVF coils.

Interestingly, figure 16 reveals an intriguing trend: the level of RE losses decreases for different plasma equilibria in the same sequential order as the decrease in their q profile in the plasma region $\psi_N > 0.7$, as depicted in figure 4. The plasma equilibrium g-24976 at 10 ms, with the highest q profile in the plasma region $\psi_N > 0.7$, exhibits the highest RE loss, exceeding 90%. Conversely, the case of plasma equilibrium g-28020 at 34 ms, with the lowest q profile in the plasma region $\psi_N > 0.7$, demonstrates a significantly lower level of experimental RE losses. Therefore, it is evident that the plasma equilibrium configuration, specifically at the plasma edge characterized by the safety factor q in the region $\psi_N > 0.7$, plays a significant role in determining the resultant RE deconfinement achieved in both experiments and simulations.

This is because the intricate drifts experienced by the REs are inherently influenced by the magnetic field topology through which they traverse and the q profiles characterize such configurations of magnetic field topology in plasma equilibria. The safety factor q is inversely proportional to the poloidal field (PF); thus with fixed B_T , a lower q corresponds to a larger PF, which causes the REs to be better confined in the plasma, resulting in a lower REs loss rate in that case. For a higher q , the PF is relatively lower, allowing REs to exhibit excursions from the originating surface, resulting in deconfinement of such REs depending on their energy and the resultant perturbation configuration in the plasma.

6. Discussion and conclusion

The present article explores the impact of magnetic field perturbation applied in the LVF configuration on RE dynamics.

RE dynamics, and subsequent deconfinement of REs in general, dominated by drift orbit excursions and subsequent losses under the influence of external magnetic field perturbations, were investigated and reported in previous works discussed in section 1. It was also reported that collisions do not play a significant role in the loss rate of the REs, as the gyration time scale 10^{-12} s and the loss rate time scale 10^{-6} s are several orders smaller than the collisional thermalisation time scale of 10^{-2} s and the effect of synchrotron radiation in RE dynamics is only significant for REs with energies >50 MeV and larger pitch angles $>40^\circ$. Hence, in the case of low-energy REs (<5 MeV in ADITYA) deconfinement using LVF perturbation would be dominated by losses from the the drift orbit excursion lead. Although the role of complex MHD activities [25, 29, 30] in expelling REs from the plasma core region to the edge region during plasma discharges cannot be neglected in actual experimental scenarios, to incorporate such intricate physical phenomena in the calculation would require more complex simulation studies [19–23, 52] that are outside the scope of the present paper. Therefore, the simulation results presented here are based on drift orbit topology analysis only.

The simulation studies were carried out using the 3D relativistic full orbit following code PARTICLE-3D (P3D), capable of taking the plasma equilibrium field as the input in standard g-file format, integrated with the EFIGI code to incorporate actual fields from various coil systems of a tokamak including the LVF coils. For benchmarking, studies of energy and momentum conservation and drift orbit topology were performed using P3D and are presented in section 3. In the simulation studies, the IPREQ-generated plasma equilibrium field configuration of ADITYA was used to study RE drift orbit dynamics and the subsequent losses of REs with different energies, the pitch angle of the REs and different directions and magnitudes of the LVF perturbation.

The simulations revealed that, unlike previously reported RE loss case studies involving RMP perturbations [18–25], LVF perturbation does not exhibit any island formation at the edge region of the RE drift orbit topology, rather it bunches and shifts the drift orbits located in different plasma regions, and the REs migrate across the plasma regions due to the complex drifts they experience, as discussed in section 4. Results obtained from both simulation and experiments, demonstrate that, in addition to the magnitude, the direction of the LVF perturbation plays an important role in RE dynamics and subsequently in determining the amount of RE loss. The prime importance of the direction of the external magnetic field perturbation applied to extract the REs in the experiments is only captured in the simulation presented here. This is in contrast to the radial diffusion theory, which is not able to explain the dependence of RE extraction on the direction of the applied perturbation field as proposed in earlier works [27, 28].

Apart from the RE losses in connection with shrinkage of confinement volumes for the case with no applied LVF (prompt loss), REs with higher energies exhibit faster deconfinement compared with their counterparts under the influence of negative LVF perturbation, as detailed in section 5. Temporal map analysis of the orbiting times of REs reveals

that REs originating from different plasma locations have different orbiting times even though they originate from the same plasma zone characterized by ψ_N , which could be attributed to the unique configuration of the LVF perturbations discussed in section 5.2. Along with the Poincaré section plots and loss fraction studies, a temporal map analysis of orbiting times, which gives insights into whether a particular RE is pushed towards the core or pulled towards the edge from its point of origin, could be used in future to design and optimise the required perturbation field configuration in any tokamak. Simulation results indicate that, as particle drifts by their inherent nature are dependent on the magnetic field configuration they experience, the negative LVF perturbation configuration of magnitude $\delta B_z/B_T \sim 10^{-2}$, which corresponds to a positive $\delta B_r/B_t \sim 10^{-3}$ and negative $\delta B_p/B_p \sim 10^{-1}$ on the inboard side of the plasma region, combined with the plasma equilibrium configuration characterized by a higher q in the edge plasma region $\psi_N > 0.7$, provides favorable conditions for achieving good RE deconfinement in both simulations and experiments, as detailed in section 5.3. In conclusion, the simulation results presented here for RE deconfinement studies in ADITYA are in alignment with the corresponding experimental findings reported earlier, and can be further extended to the the recent experimental observations in future.

Along with other RE mitigation methods, LVF perturbation-assisted RE mitigation may be envisioned as an additional technique for suppression or mitigation of REs in larger tokamaks such as ITER. Based on the LVF assisted experiments in ADITYA [27, 28] and the simulation results presented in this paper, a threshold magnitude of LVF perturbation of 3%–4% of the toroidal magnetic field is required for effective RE mitigation. Qualitatively, for the ITER design parameter of $B_T = 5.3$ T, a threshold LVF perturbation field of $\sim 2\text{--}2.5$ kG would be required at the plasma centre in ITER. This field perturbation at one toroidal location can be generated through a suitably designed coil. Note that the precise threshold values of the LVF perturbation required for RE mitigation in any tokamak can be estimated using the simulations presented in this article. Furthermore, the proposed technique may be advantageous for mitigating disruption-generated REs as well. Firstly, the relatively higher resistance of the post-disruptive plasmas would facilitate penetration of the LVF into the plasma; secondly, longer pulse durations of the LVF perturbations may be used because in disruption phase degradation of the main plasma due to the perturbation field is not a concern. This suggests that the reported technique of RE mitigation through the application of a LVF is quite feasible in bigger tokamaks including ITER and can also be used in synergy with massive gas or pellet injection techniques to enhance runaway losses before they gain higher energies. Moreover, relatively simpler implementation of the LVF perturbation-assisted RE mitigation technique may also be used in real-time feedback mode [27]. Note that although the extrapolation of this proposed RE mitigation technique in bigger tokamaks including ITER is feasible, more experiments in existing tokamaks are required along with suitable amendments in the presented simulation considering the effects of relatively large toroidal fields, collisions and radiation. This

remains as a work to be done and will be presented in a future publication.

Acknowledgments

The authors would like to thank Lt Dr R. Srinivasan for his insightful guidance and advice during the development of the code. This work was performed at the HPC facility ANTYA of the Institute for Plasma Research, Gandhinagar, India. Finally, the authors would like to thank Mr Deepak Aggarwal for his help and support in resolving HPC-related issues encountered during the execution of the code on ANTYA.

ORCID iDs

Someswar Dutta  <https://orcid.org/0009-0001-0706-2357>
R.L. Tanna  <https://orcid.org/0000-0003-4613-7072>

References

- [1] Lehnens M. *et al* 2015 *J. Nucl. Mater.* **463** 39
- [2] Hollmann E.M. *et al* 2015 *Phys. Plasmas* **22** 021802
- [3] Hender T.C. *et al* 2007 *Nucl. Fusion* **47** S128–202
- [4] Boozer A.H. *et al* 2015 *Phys. Plasmas* **22** 032504
- [5] Knoepfel H. and Spong D.A. 1979 *Nucl. Fusion* **19** 785–829
- [6] Rasouli C., Iraji D., Farahbod A.H., Akhtari K., Rasouli H., Modarresi H. and Lamehi M. 2009 *Rev. Sci. Instrum.* **80** 013503
- [7] Sharma A.S. and Jayakumar R. 1988 *Nucl. Fusion* **28** 491
- [8] Reux C. *et al* 2022 *Plasma Phys. Control. Fusion* **64** 034002
- [9] Saint-Laurent F. *et al* 2013 *Fusion Sci. Technol.* **64** 711–8
- [10] Banerjee S. *et al* 2021 *Nucl. Fusion* **61** 016027
- [11] Putvinski S., Barabaschi P., Fujisawa N., Putvinskaya N., Rosenbluth M.N. and Wesley J. 1997 *Plasma Phys. Control. Fusion* **39** B157
- [12] Yoshino R. and Tokuda S. 2000 *Nucl. Fusion* **40** 1293
- [13] Lehnens M., Bozhenkov S.A., Abdullaev S.S. and Jakubowski M.W. 2008 *Phys. Rev. Lett.* **100** 255003
- [14] Lehnens M. *et al* 2009 *J. Nucl. Mater.* **390–391** 740–6
- [15] Finken K. *et al* 2006 *Nucl. Fusion* **46** S139
- [16] Finken K., Abdullaev S.S., Jakubowski M.W., Jaspers R., Lehnens M., Schlickeiser R., Spatschek K.H., Wingen A. and Wolf R. (the TEXTOR Team) 2007 *Nucl. Fusion* **47** 91
- [17] Ghendrih P., Grosman A. and Capes H. 1996 *Plasma Phys. Control. Fusion* **38** 1653
- [18] Papp G., Drevlak M., Fülöp T. and Helander P. 2011 *Nucl. Fusion* **51** 043004
- [19] Gobbin M. *et al* 2018 *Plasma Phys. Control. Fusion* **60** 014036
- [20] Gobbin M., Marrelli L., Valisa M., Li L., Liu Y.Q., Papp G., Pautasso G. and McCarthy P.J., (ASDEX Upgrade Team and EUROfusion MST1 Team) 2021 *Nucl. Fusion* **61** 066037
- [21] Ficker O. *et al* 2019 *Nucl. Fusion* **59** 096036
- [22] Liu Y., Paz-Soldan C., Macusova E., Markovic T., Ficker O., Parks P.B., Kim C.C., Lao L.L. and Li L. 2020 *Phys. Plasmas* **27** 102507
- [23] Izzo V.A., Puszta I., Särkimäki K., Sundström A., Garnier D.T., Weisberg D., Tingueley R.A., Paz-Soldan C., Granetz R.S. and Sweeney R. 2022 *Nucl. Fusion* **62** 096029
- [24] Riccardo V. *et al* 2010 *Plasma Phys. Control. Fusion* **52** 124018
- [25] Papp G., Drevlak M., Fülöp T., Helander P. and Pokol G.I. 2011 *Plasma Phys. Control. Fusion* **53** 095004
- [26] Stone D.S. and Richards B. 1978 *Phys. Fluids* **21** 149–50
- [27] Tanna R.L. *et al* 2015 *Nucl. Fusion* **55** 063010
- [28] Tanna R.L. *et al* 2023 *Nucl. Fusion* **63** 086011
- [29] Helander P., Eriksson L.-G. and Andersson F. 2000 *Phys. Plasmas* **7** 4106
- [30] Rechester A.B. and Rosenbluth M.N. 1978 *Phys. Rev. Lett.* **40** 38
- [31] Raj H. *et al* 2018 *Nucl. Fusion* **58** 076004
- [32] Fussmann G. 1979 *Nucl. Fusion* **19** 327
- [33] Martin-Solis J.R., Alvarez J.D., Sanchez R. and Esposito B. 1998 *Phys. Plasmas* **5** 2370
- [34] Rosenbluth M.N. and Putvinski S.V. 1997 *Nucl. Fusion* **37** 1355
- [35] Heikkinen J.A. and Sipila S.K. 1993 *Comput. Phys. Commun.* **76** 215
- [36] Eriksson L.G. and Helander P. 2003 *Comput. Phys. Commun.* **154** 175
- [37] Landreman M., Stahl A. and Fülöp T. 2014 *Comput. Phys. Commun.* **185** 847
- [38] Stahl A., Hirvijoki E., Decker J., Embreus O. and Fülöp T. 2015 *Phys. Rev. Lett.* **114** 155002
- [39] Aleynikov P. and Breizman B.N. 2015 *Phys. Rev. Lett.* **114** 155001
- [40] Nilsson E., Decker J., Peysson Y., Granetz R.S., Aint-Laurent F. and Vlainic M. 2015 *Plasma Phys. Control. Fusion* **57** 095006
- [41] Guan X., Qin H. and Fisch N.J. 2010 *Phys. Plasmas* **17** 092502
- [42] Russo A.J. 1991 *Nucl. Fusion* **31** 117
- [43] Jian L., Yulei W. and Hong Q. 2016 *Nucl. Fusion* **56** 064002
- [44] Yulei W., Hong Q. and Jian L. 2016 *Phys. Plasmas* **23** 062505
- [45] Carbajal L., Del-castillo-negrete D., Spong D., Seal S. and Baylor L. 2017 *Phys. Plasmas* **24** 042512
- [46] Dutta S *et al* 2019 *Plasma Sci. Technol.* **21** 105101
- [47] Srinivasan R. 2002 Study of high beta compact toroidal configurations *PhD Thesis* Institute for Plasma Research
- [48] Sharma D., Srinivasan R., Ghosh J. and Chattopadhyay P. 2020 *Fusion Eng. Des.* **160** 111933
- [49] Sackett S.J. 1978 EFFI: a code for calculating the electromagnetic field, force, and inductance in coil systems of arbitrary geometry
- [50] Hoppe M., Ekmek I., Berger E. and Fülöp T. 2022 *J. Plasma Phys.* **88** 905880317
- [51] Vay J.-L. 2008 *Phys. Plasmas* **15** 056701
- [52] Izzo V.A. *et al* 2011 *Nucl. Fusion* **51** 063032